Velocity structure above seismological bedrock estimated from earthquake recordings: an application of diffuse wave-field concept to strong motions in Iran

Iman Ashayeri[1*] , Eri Ito[2] and Hiroshi Kawase[2]

Abstract

We present velocity structure inversion for three stations of Iranian Strong Motion Network (ISMN), and one KiK-net station that is used as a benchmark, for the application of diffuse wave-field concept in tectonic and geological setting of the west of Iran. This study compares the results of two existing computer codes for the velocity structure inversion at these sites. The computer codes use different search space parameterization, and error-minimization algorithms. Firstly, the available information on subsurface structure and surface geology from the strong motion stations is introduced. Then, ground motions of M_W larger than 4, with PGA of all components less than 50 cm/s^2 are used to calculate horizontal-to-vertical spectral ratios of earthquakes (eHVSR) at each station. The observed eHVSR curves are inverted for the velocity structure of the stations, and the results are compared with each other and the information of previous studies. Finally, the eHVSR curves of the mainshock records of the recent M_W 7.3 earthquake at two ISMN sites are investigated. The velocity inversion is repeated by considering the shear modulus degradation of several shallow layers. Empirical nonlinear site amplification functions are calculated based on the modified V_S structure and the V_S structure of the linear ground response for two ISMN stations.

Keywords Diffuse field concept, Earthquake horizontal-to-vertical spectral ratio, Velocity structure inversion, Nonlinear site amplification function

*Correspondence:
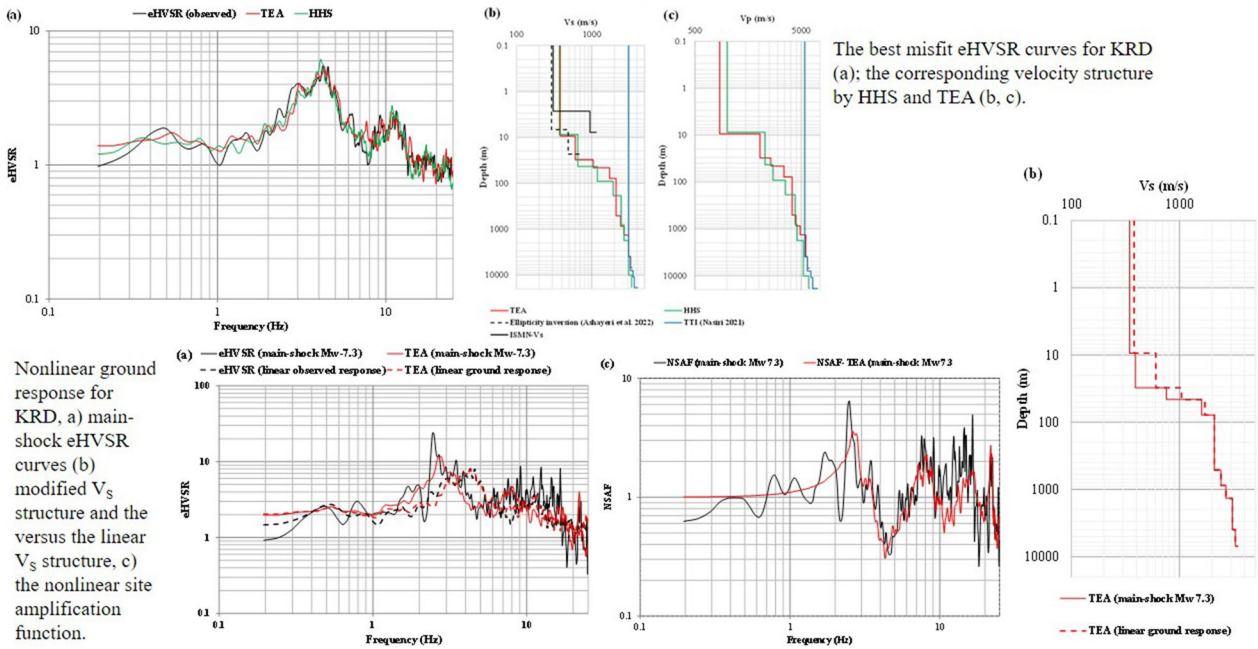Iman Ashayeri
i.ashayeri@razi.ac.ir
Full list of author information is available at the end of the article

Ashayeri *et al. Earth, Planets and Space*   (2023) 75:94

Page 2 of 17

Graphical Abstract

Velocity structure above seismological bedrock estimated from earthquake recordings; an application of diffuse wave-field concept to strong motions in Iran

Introduction

A diffuse wave-field refers to a wave-field where at any point is an isotropic random superposition of plane waves (Weaver 1982). Egle (1981) studied the diffuse wave-field in solid media and concluded that the diffuse wave-field will have its energy partitioned between transverse and longitudinal waves, depending only on the Poisson ratio (Weaver 1985). Egle (1981) also showed that for an impulsive source, the diffuse wave-field is observed after a relatively short time, regardless of the partition of the energy densities at the source.

Sanchez-Sesma et al. (2011a) applied the diffuse wave-field concept for microtremors recorded by a single station. They considered that the microtremor is contributed by all types of waves (i.e., body waves and surface waves) that are originated from randomly distributed point sources on the surface, and forms a diffuse wave-field. Furthermore, they introduced that the spectral ratio of horizontal-to-vertical motions on the surface is related to the directional energy densities of the horizontal and vertical motions, or eventually the imaginary parts of the Green's functions of horizontal and vertical directions for a point source in the same direction on the surface. Sanchez-Sesma et al. (2011b) established the relationship between the Green's function and average correlations of motions.

Kawase et al. (2011) investigated earthquake motions for validation of the diffuse wave-field concept, and they found that the horizontal-to-vertical spectral ratio of a few hundred synthetics with the variety of inclined incidences and azimuths matches the diffuse wave-field concept. This finding gives the ratio of the Green's functions components in terms of the ratio of transfer functions of vertically incident plane S- and P-waves from seismological bedrock. The relationships in Sanchez-Sesma et al. (2011a) and Kawase et al. (2011) provided equations for the velocity structure inversion of the ground layers, which are represented in Eqs. 1 and 2, respectively:

$$\left[\frac{H}{V}\right](\omega) = \sqrt{\frac{[NS(\omega)]^2 + [EW(\omega)]^2}{[UD(\omega)]^2}} = \sqrt{\frac{2Im[G_{11}(x,x,\omega)]}{Im[G_{33}(x,x,\omega)]}},$$
(1)

$$\left[\frac{H}{V}\right](z,\omega) = \sqrt{\frac{[NS(\omega)]^2 + [EW(\omega)]^2}{[UD(\omega)]^2}} = \sqrt{\frac{2\alpha_{SB}}{\beta_{SB}}\frac{|TF_1(z,\omega)|}{|TF_3(z,\omega)|}},$$
(2)

where the left-hand sides (LHS) of Eqs. 1 and 2 are the average spectral ratio of the horizontal and vertical motions of microtremor at surface point of x, and the average spectral ratio of the horizontal and vertical

Ashayeri *et al. Earth, Planets and Space*   (2023) 75:94

Page 3 of 17

motions of earthquakes (eHVSR) at a given depth z, respectively. Analogously, the right-hand sides (RHS) of Eqs. 1 and 2 are the square root of summation of the imaginary parts of the Green's functions in the horizontal directions for source and receiver at point x divided by the imaginary part of the Green's function in the vertical direction of the microtremor motions at the same point, and the ratio of the absolute summation of S-wave transfer function divided by the absolute P-wave transfer function of earthquake motions at a given depth z corrected for the square root of the ratio of α_{SB} and β_{SB} as the P-wave and S-wave velocities of the seismic bedrock to account for the energy partition at the seismological bedrock, respectively.

The RHS of Eq. 1 was resolved by Garcia-Jerez et al. (2013) as an integral on the complex wave-number plane for separate contributions of body waves and surface waves of Rayleigh and Love types. In this way, Garcia-Jerez et al. (2016) developed a computer code to perform velocity structure inversion by optimizing the error between LHS and RHS of Eq. 1 for a potential solution. The RHS of Eq. 2 was resolved by Kawase et al. (2011) for the calculation of S-wave and P-wave transfer functions and Nagashima et al. (2014) applied the idea of the genetic algorithm with the simulated annealing from Yamanaka (2007) that is named hybrid heuristic search (HHS), to make the velocity structure inversion possible from earthquakes. Recently, Ashayeri et al. (2023) developed a new evolutionary algorithm, called telescopic evolutionary algorithm (TEA), to perform the velocity structure inversion, based on the diffuse wave-field concept of Kawase et al. (2011).

The inversion of eHVSR for velocity structure was examined for several stations of K-NET and KiK-net, operated by NIED, Japan (Aoi et al. 2020 and data from NIED 2019); as in Nagashima et al. (2014), Kawase et al. (2018a), Nagashima and Kawase (2019), and Ashayeri

et al. (2023). The current study examines the two optimization algorithms of Nagashima et al. (2014) and Ashayeri et al. (2023), namely HHS and TEA, respectively, on three stations of Iranian Strong Motion Network (ISMN 2022), to investigate the application of diffuse wave-field in a different tectonics and geology, and to compare the performance of HHS and TEA in the error optimization. Moreover, one KiK-net station (IBRH11) is investigated in this study as a benchmark for the validation of HHS and TEA under similar conditions as much as possible. In the following sections, firstly, the strong-motion stations are introduced and eHVSR curves are presented for the linear ground response. Secondly, we apply HHS and TEA for the velocity structure inversion at three stations of ISMN. We also present the comparison at one station of KiK-net. Finally, soil nonlinearity during the mainshock of a recent earthquake in Iran is investigated by introducing eHVSR curves of the nonlinear ground response at two ISMN stations, where the observed PGAs exceeded 250 cm/s^2. The discussions and conclusions about the results come afterwards.

Strong motion stations and observed eHVSR

In this study, three strong-motion stations of ISMN namely KRD, SLS, SPZ, and one KiK-net station namely IBRH11 as a benchmark are investigated. IBRH11 was selected because it was investigated in detail by Satoh et al. (2014) after the 2011 Off the Pacific Coast of Tohoku earthquake. Table 1 presents the coordinates as well as the surface geological units for these stations. Furthermore, Fig. 1 shows the locations of ISMN's stations along with the seismic fault-lines on a map of the region.

NIED (2019) gives soil condition for IBRH11 down to a depth of 103 m based on the downhole test. ISMN (2022) gives only PS-logs for KRD, SLS, and SPZ from the seismic refraction tests. However, Ashayeri et al. (2022) measured microtremors at KRD and SPZ and performed

Table 1 The strong motion stations of this study

Station	Latitude	Longitude	Province/prefecture	Sensor depth (m)	Surface geology[a]
KRD	34.2802	46.2408	Kermanshah	$Z=0$	Q^{t2}: Quaternary young alluvial terrace
SLS	34.7432	46.1505			Q^t: Quaternary fan and alluvial plain
SPZ	34.4554	45.8699			Qt: Quaternary coarse and fine grain alluvium Bk: Pliocene thin bedded to massive consolidated conglomerate, Bakhtyari formation
IBRH11	36.3701	140.1401	Ibarakiken	$Z=0, 103$	a: Quaternary, Holocene gravel, sand and mud alluvium Sk: Quaternary, Middle Pleistocene gravel, sand and mud, Sakaibayashi formation

[a] The reference is either Geological Survey and Mineral Exploration of Iran or Geological Survey of Japan
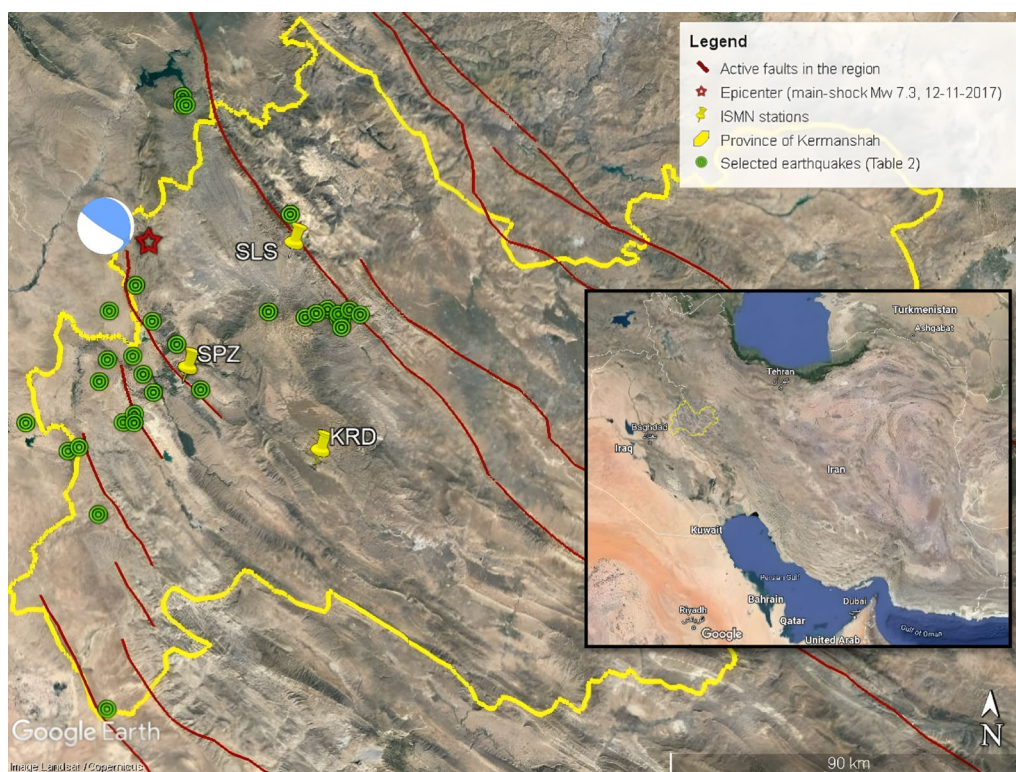
Fig. 1 The locations of ISMN stations, epicenters of the selected earthquakes, active faults in the region, and the focal mechanism of the 12 November 2017 mainshock on the map of Kermanshah province, and the map of the country

inversion analyses for the velocity structures of shallow depth. Similar to the methods that were applied by Konno and Ohmachi (1998), Satoh et al. (2001), Arai and Tokimatsu (2004), Fäh et al. (2009), and Hobiger et al. (2009, 2013), the ellipticity curve of Rayleigh wave from the microtremors were used for the inversion analyses in Ashayeri et al. (2022). Figure 2a–d represents the shear wave velocity profiles of the four stations based on the previous investigations. The discrepancy between the seismic refraction PS-log and the velocity structure inversion of the ellipticity curve at KRD and SPZ was interpreted by Ashayeri et al. (2022), because of a large distance between the stations and the seismic refraction tests. Interestingly, the current study can support this interpretation by providing the velocity structures from the inversion of eHVSR at KRD and SPZ.

The observed eHVSR for each station is calculated based on a 40.96 s (or 20.48 s) time-window from the S-wave onset of earthquake records with Mw greater than 4 and PGA of all components less than 50 cm/s². Therefore, it is considered as the linear response of the ground structure of the basin from the seismic bedrock to the surface. Table 2 lists the selected earthquakes with their magnitude, focal depth, and epicentral distance to the ISMN stations. The epicenters of the selected

earthquakes are shown in Fig. 1. Each qualified earthquake record is processed for baseline correction and filtering by a band-pass Butterworth filter of 4th order, and a frequency band from 0.1 to 25 Hz, before taking a fast Fourier transform. All the Fourier transformed motions are smoothed by Parzen window with a width of 0.1 Hz (or 0.2 Hz in case of a 20.48-s time-window). The geometrical average of 10 transformed motions usually presents a stable eHVSR curve. Thereby, eHVSR curves of the observed ground response of Fig. 3 are prepared for a reliable frequency range from 0.2 to 25 Hz for KRD, SLS, and SPZ or from 0.1 to 20 Hz for IBRH11.

Referring to Eq. 2, it is common to calculate a separated directional spectral ratio (i.e., NS/UD and EW/UD), to observe any possible 2D-basin effects (Matsushima et al. 2017). If there is no distinction between the directional spectral ratios at each station (i.e., NS/UD is similar to EW/UD), either a vector magnitude of two horizontal directions (like in Eq. 2) or a root mean square (RMS) of the horizontal directions (i.e., $\sqrt{\frac{NS^2+EW^2}{2(UD^2)}}$) is calculated, and is used as the target eHVSR for the inversion analysis. One must remember, if an RMS of eHVSR or a directional eHVSR (i.e., NS/UD or EW/UD) is used for the LHS of Eq. 2, the multiplier of 2 in the RHS of Eq. 2 must
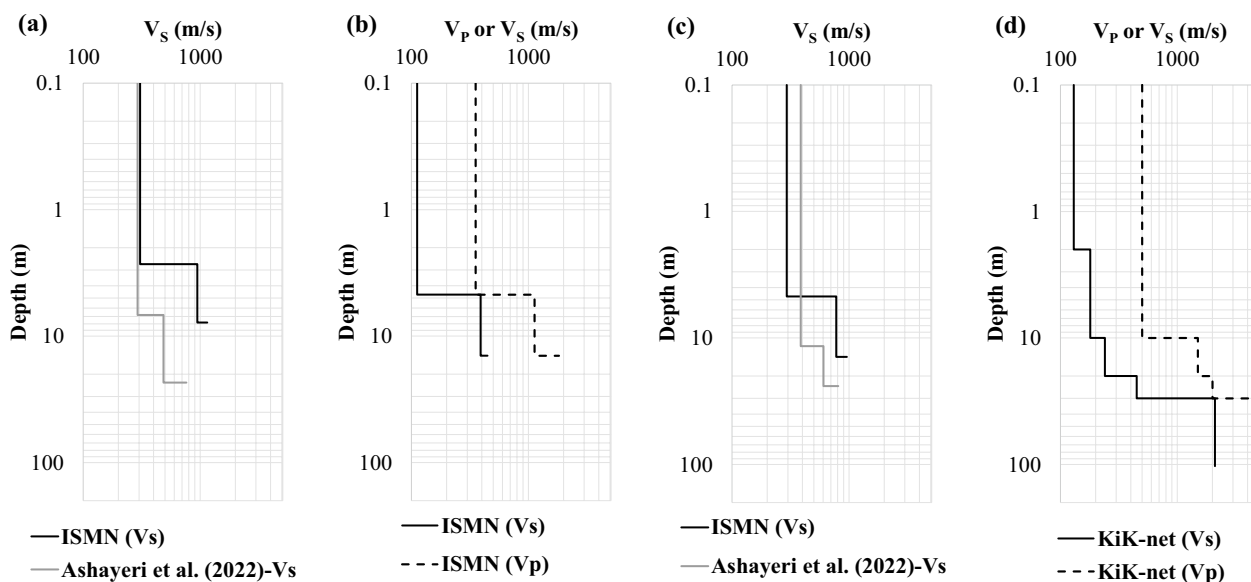
Ashayeri *et al. Earth, Planets and Space* (2023) 75:94

Page 5 of 17

Fig. 2 The velocity structure from KiK-net, ISMN, and previous studies. **a** KRD, **b** SLS, **c** SPZ, **d** IBRH11; No reliable VP profile was available to report for KRD, and SPZ

be replaced with 1, because the RHS of Eq. 2 is subsequently, either the RMS of transfer functions in horizontal directions, or the transfer function of the single horizontal direction in the LHS (i.e., NS or EW). Figure 3a–d presents eHVSR curves of the observed ground response at KRD, SLS, SPZ, and IBRH11, respectively. It is observed that the directional eHVSR curves of each station are similar. However, in KRD and SPZ there are slight distinctions between NS and EW directions, at low and high frequencies, respectively, which are ignored in this study.

On November 12, 2017, an earthquake event of Mw 7.3 happened in Kermanshah province, Iran, the epicenter of which was close to the ISMN stations of KRD, SLS, and SPZ (see Fig. 1). Nissen et al. (2019) characterized the rupture mechanism, aftershock sequence, background seismicity, and regional tectonics of the event. The local site-effect at the most damaged city of Sarpol-e-zahab was investigated by Ashayeri et al. (2020 and 2021), and the damage levels of the buildings from the inventory survey were studied by Biglari and Formisano (2020) and Biglari et al. (2021). Fortunately, the mainshock was recorded at KRD and SPZ with PGAs equal to 261 (from EW-component) and 684 (from NS-component) cm/s^2, respectively. Hereby, we investigated the soil nonlinearity in the shallow ground structure at KRD and SPZ by comparing the eHVSR of the mainshock with the eHVSR of the linear ground response as previous studies such as Wang et al. (2021) had reported. Eventually, we presented the possible velocity structure corresponding to

the degradation of shear modulus. Figure 4a–b presents the eHVSR of the mainshock at KRD and SPZ, respectively. As an example, Fig. 4c presents the three-component acceleration time-history of the mainshock at SPZ, and the red part is the time-window that was used for the calculation of eHVSR of the mainshock. It is helpful to recall that for all selected earthquakes in Table 2, we used a 20.48-s time-window just after the S-wave arrival to calculate the eHVSR of the linear ground response. The comparison with the eHVSR of the linear ground response reveals shifting of peak frequencies to lower values along with the amplitude amplification or de-amplification.

The velocity structure inversion

As for a velocity structure inversion, two available codes of Nagashima et al. (2014) and Ashayeri et al. (2023) are used. Both codes use a similar direct problem solver to calculate the theoretical eHVSR based on DFC. This is demonstrated in Fig. 5 for IBRH11, where the codes present the theoretical eHVSR of a given ground structure defined by thickness, V_S, V_P, density, and damping ratio of each layer. As we can see, both codes provide an identical eHVSR curve. This example validates the uniqueness of the direct-problem solutions of the codes.

The difference between the codes is in the searching algorithm and the error minimization procedure. The former code (Nagashima et al. 2014) uses HHS, which starts up with a given number of randomly generated ground profiles based on an initial ground profile and

Ashayeri *et al. Earth, Planets and Space*   (2023) 75:94

Page 6 of 17

Table 2 The characteristics of the selected earthquakes that are used for the calculation of eHVSR at each station

Event (date and time GMT)	Magnitude (M_W)	Focal depth (km)	Epicentral distance (km)		
			KRD	SLS	SPZ
22/11/2013 (06:51:24)	5.6	10	74	–	–
22/11/2013 (18:30:57)	5.7	10	62	–	–
24/11/2013 (18:05:42)	5.5	14	60	–	–
12/11/2017 (21:33:21)	4.5	11	–	–	18
12/11/2017 (22:31:00)	4.6	11	–	–	26
12/11/2017 (23:37:22)	4.3	6	–	14	–
15/11/2017 (07:11:20)	4.0	9	–	–	10
19/11/2017 (01:07:33)	4.3	8	–	–	5
20/11/2017 (15:36:54)	4.5	8	–	39	–
06/12/2017 (05:53:44)	4.9	8	–	49	–
06/12/2017 (07:57:41)	4.4	14	–	–	20
11/12/2017 (14:09:57)	5.4	8	–	47	–
11/12/2017 (14:42:41)	4.7	6	–	47	–
26/12/2017 (09:11:31)	4.4	8	–	11	–
06/01/2018 (15:22:08)	5.1	6	49	–	–
11/01/2018 (06:59:29)	5.5	8	–	–	84
01/04/2018 (08:35:25)	5.2	7	45	–	–
22/07/2018 (10:07:25)	5.7	8	39	–	41
22/07/2018 (16:48:47)	4.2	6	–	22	–
23/07/2018 (00:59:47)	4.5	6	–	20	–
25/07/2018 (01:47:47)	4.2	9	–	20	–
04/08/2018 (17:02:04)	4.2	8	–	23	–
25/08/2018 (22:13:25)	6.0	8	–	–	38
26/08/2018 (09:23:33)	4.5	7	36	–	–
29/08/2018 (05:34:35)	4.6	8	–	20	–
05/11/2018 (20:32:07)	4.4	8	–	19	–
25/11/2018 (16:37:31)	6.3	11	50	59	–
26/11/2018 (00:38:36)	5.1	8	47	–	–
09/12/2018 (03:24:11)	4.5	10	–	–	16
06/01/2019 (13:41:59)	5.7	11	57	–	40
15/04/2019 (06:34:31)	4.4	11	–	–	14
05/06/2019 (03:36:16)	4.9	9	–	–	21
12/11/2017 (18:18:16)[a]	7.3	18	70	–	36
No. of earthquakes			*10*	*13*	*12*
Range of magnitude			*4.5–6.3*	*4.2–6.3*	*4–6*
Range of epicentral distance (km)			*36–74*	*11–59*	*5–84*

[a] Just used for calculation of nonlinear eHVSR

given ranges for the ground layers' parameters. It proceeds with producing a next generation by selecting parents and applying cross-over and mutation, and then checking a pass-over probability for the child and parents. Finally, it stops after a given number of generations. In this study, the population of each generation was set to 400, and the algorithm run for 200 generations. The later code (Ashayeri et al. 2023) uses TEA, in which the optimization of solutions is performed in steps, with a descending population of potential solutions, and the selection of the solutions that are transferred to the next step, is based on a descending error threshold from the first step to the last step of the algorithm. Hence, TEA starts up with a number of randomly generated ground profiles within a given search space of parameters for each ground layer. The number of population is equal to $N_\mathrm{P} \times d^\mathrm{n}$, where N_P is the number of optimal profiles, n is the number of steps, and d is the population descending
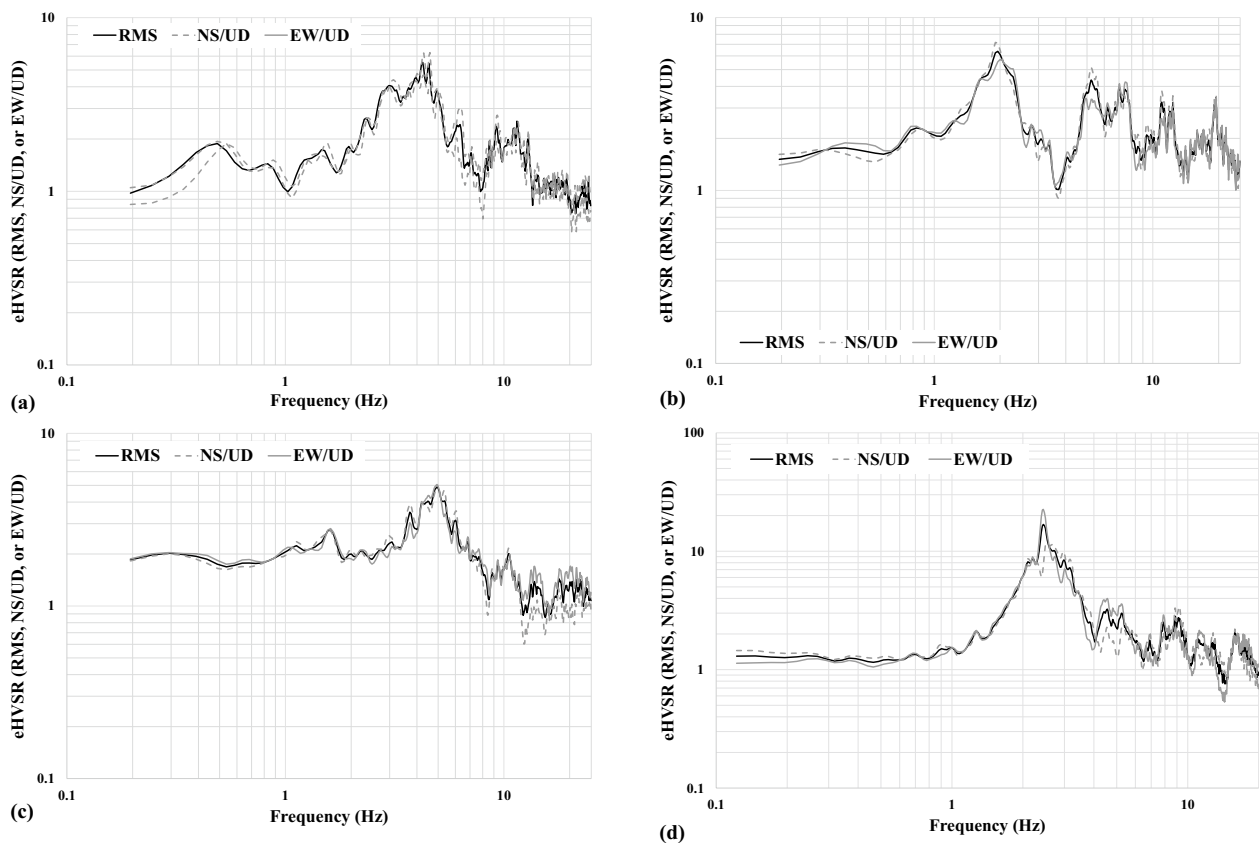
Fig. 3 The observed eHVSR curves from earthquake records, **a** KRD, **b** SLS, **c** SPZ, and **d** IBRH11

ratio. It proceeds to the next step with producing a next generation of a smaller population (i.e., $N_P \times d^{n-1}$), from the children, which all have a smaller misfit. Finally, it stops in the last step with finding N_P individuals all having a misfit smaller than a given threshold (Ashayeri et al. 2023). The start-up parameters were $N_P = 50$, $n = 3$, and $d = 5$ in this study.

In both codes, it is possible to apply predefined correlations for V_S–V_P, V_S–density, and V_S–damping ratio for each layer. In this way, the main optimization is handled on the thickness and V_S of the layers. The initial ground profile in the code of Nagashima et al. (2014) is defined with a median and a coefficient of variation for each variable; while it is required to define a range for each variable in the code of Ashayeri et al. (2023). We tried to define similar initial states and overlapping search spaces for each inversion problem in the codes, to have a fair comparison between the codes. The initial states and the search spaces are introduced in Table 3 in terms of the thickness and V_S of each layer. As for the other parameters, the correlations in Table 4 were used by HHS and TEA from Nagashima and Kawase (2021) and Ashayeri et al. (2023), respectively. It is worth noting that viscous damping was used to calculate the complex values of

V_S and V_P from the complex shear modulus, defined as $G^* = G(1 + 2Di)$ with D standing for the damping ratio. Furthermore, the damping ratio was assumed frequency-dependent for KRD, SLS, and SPZ, but frequency-independent for IBRH11.

The results of the least misfit eHVSR curves of KRD, SLS, SPZ, and IBRH11 are presented in Figs. 6, 7, 8, 9a for both codes. Furthermore, the velocity structure of the least misfit curve is shown in Figs. 6, 7, 8, 9b and c, respectively. In terms of eHVSR curves both codes were satisfactorily successful to capture all peaks and troughs at the entire frequency range for all stations. The velocity structure at each station is demonstrated by V_S and V_P profiles. It is acceptable that an eHVSR curve is mostly controlled by the thickness and V_S of the layers. It is also acceptable that for most of the cases the impedance contrast of S-waves between layers is larger than that of P-waves. Hence, V_P is considered less effective than thickness and V_S in forming the frequency and amplitude of the peaks of an eHVSR curve. The damping ratio is also effective in the amplitude of the peaks of an eHVSR curve.

For the three ISMN stations, both HHS and TEA were able to successfully capture the observed eHVSR curves.
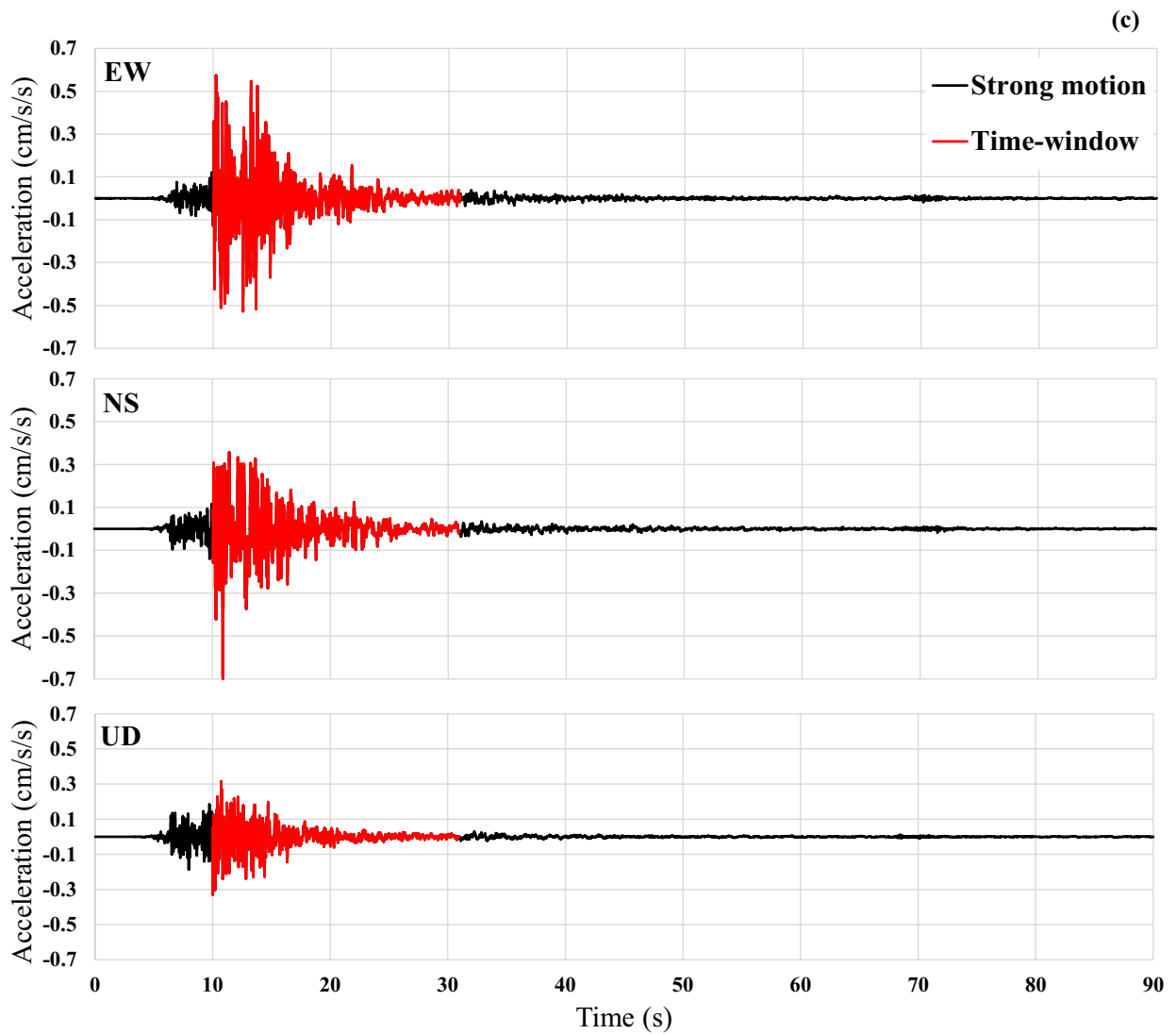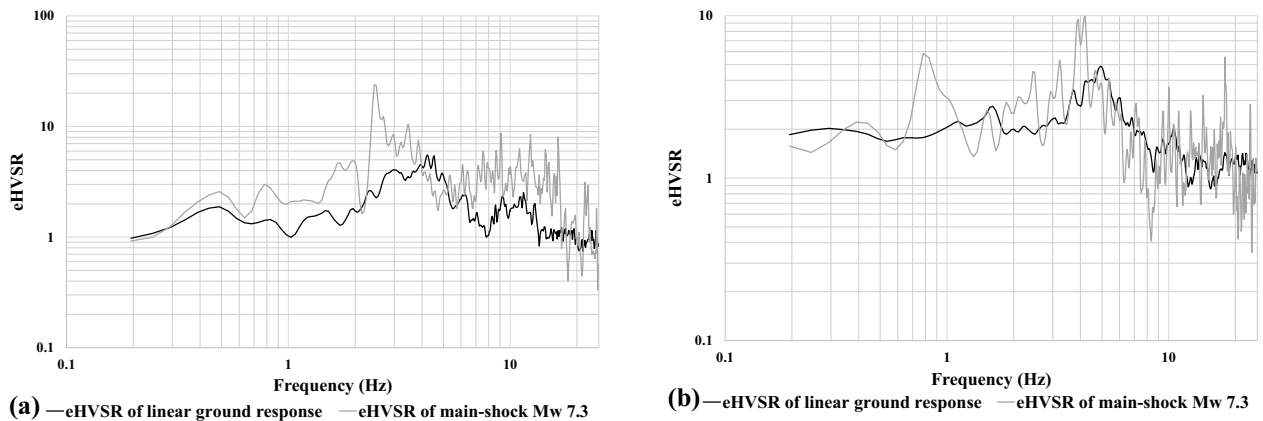
Fig. 4 The comparisons of eHVSR for the linear ground response and the mainshock of Mw 7.3 earthquake at **a** KRD, **b** SPZ, **c** The strong motion record and the selected time-window (20.96 s) for the calculation of eHVSR of the mainshock
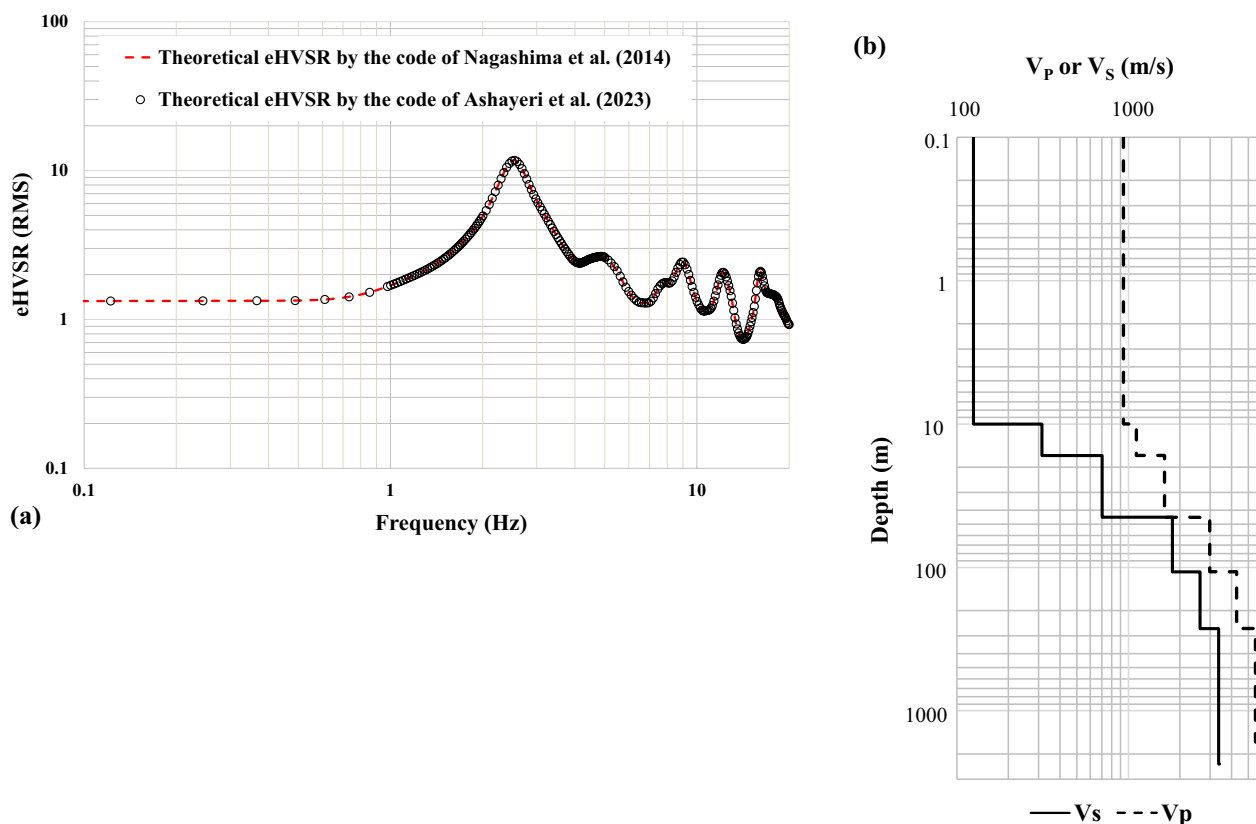
Ashayeri *et al. Earth, Planets and Space* (2023) 75:94

Page 9 of 17

Fig. 5 a The theoretical eHVSR curves by the codes of Nagashima et al. (2014) and Ashayeri et al. (2023), **b** the given velocity structure

This clearly validates the theoretical base of Eq. 2 for the tectonic and geological setting of the Kermanshah region in Iran. Although the inverted velocity structures by HHS and TEA are slightly different, both are very useful for these stations. The discrepancy may be coming from a small difference in the searching range between them around the initial information. As for the deep earth structure in the Kermanshah region, Nasiri (2021) used the Travel Time Inversion (TTI) of P- and S-wave arrival times of the mainshock as well as aftershocks after the November 12, 2017, Mw 7.3 earthquake. Obviously, TTI method gives no distinction of layers at the shallow depth. Figures 6, 7, 8b and c present the velocity structure by TTI in blue lines. The velocity structures presented by both HHS and TEA are very consistent with the one by TTI at layers deeper than 1000 m, while TEA and TTI are more consistent in terms of the depth, V_P, and V_S of the seismological bedrock. Furthermore, for KRD and SPZ the V_S-profile of the shallow layers down to the engineering bedrock was estimated by Ashayeri et al. (2022) from the inversion of the ellipticity curve of Rayleigh wave of microtremors, which are shown with a black dash-line in Figs. 6b and 8b. The V_S-profiles of their study are consistent with the V_S-profiles of this study for the shallow depth. However, the velocity structures of the current study should be considered as a more reliable structure as they are based on the inversion of eHVSR curves (including peaks, troughs, and flat parts), within a frequency range from 0.2 to 25 Hz. Comparisons between the V_S structure of this study and V_S structure reported by ISMN for KRD, SLS, and SPZ reveal that the ISMN's profiles are not accurate, and even should not be used as the shallow ground structures.

In the case of IBRH11, where a downhole test was available, HHS presents a more consistent eHVSR curve than TEA in frequencies higher than the peak frequency. Meanwhile, it seems that the velocity structure presented by TEA is more similar to the downhole test at IBRH11. It seems that TEA converged to a solution that is more consonant than HHS, with the initial model that was defined based on the downhole test.

In summary, the slight discrepancy between the inverted velocity structures by HHS and TEA, is interpreted to be from the difference in the searching range between them around the initial information; the searching range of TEA was more confined around the initial information, while the searching range of HHS was set to the initial values $\pm 100\%$ (see Table 3). Therefore, HHS

Ashayeri *et al. Earth, Planets and Space*   (2023) 75:94

Page 10 of 17

Table 3 The initial ground profile or the searching range in terms of the thickness and V_S of layers

Station	Layer	Parameter	HHS		TEA
			Initial	Range	Range
KRD	1	Thickness (m)	9.5	Initial ± 100%	7–12
		V_S (m/s)	400		350–450
	2	Thickness (m)	22.5		15–30
		V_S (m/s)	650		600–700
	3	Thickness (m)	17.5		10–25
		V_S (m/s)	1050		950–1150
	4	Thickness (m)	30		10–50
		V_S (m/s)	1700		1650–1750
	5	Thickness (m)	450		350–550
		V_S (m/s)	2075		1950–2200
	6	Thickness (m)	400		250–550
		V_S (m/s)	2325		2200–2450
	7	Thickness (m)	500		350–650
		V_S (m/s)	2575		2450–2700
	8	Thickness (m)	2500		2000–3000
		V_S (m/s)	3100		3000–3200
	9	Thickness (m)	3500		3000–4000
		V_S (m/s)	3250		3200–3300
	SB	V_S (m/s)	3400		3400–3500
SLS	1	Thickness (m)	5.5	Initial ± 100%	1–10
		V_S (m/s)	175		150–200
	2	Thickness (m)	8		1–15
		V_S (m/s)	285		220–350
	3	Thickness (m)	27.5		5–50
		V_S (m/s)	475		400–550
	4	Thickness (m)	27.5		5–50
		V_S (m/s)	700		550–850
	5	Thickness (m)	25.5		1–50
		V_S (m/s)	1100		900–1300
	6	Thickness (m)	25.5		1–50
		V_S (m/s)	1525		1350–1700
	7	Thickness (m)	175		50–300
		V_S (m/s)	1975		1750–2200
	8	Thickness (m)	325		100–550
		V_S (m/s)	2450		2200–2700
	9	Thickness (m)	550		350–750
		V_S (m/s)	2850		2700–3000
	10	Thickness (m)	6250		5500–7000
		V_S (m/s)	3150		3000–3300
	SB	V_S (m/s)	3400		3400–3500

Table 3 (continued)

Station	Layer	Parameter	HHS		TEA
			Initial	Range	Range
SPZ	1	Thickness (m)	10	Initial ± 100%	5–15
		V_S (m/s)	325		250–400
	2	Thickness (m)	15		5–25
		V_S (m/s)	500		400–600
	3	Thickness (m)	27.5		5–50
		V_S (m/s)	775		600–950
	4	Thickness (m)	150		50–250
		V_S (m/s)	1125		950–1300
	5	Thickness (m)	87.5		25–150
		V_S (m/s)	1525		1300–1750
	6	Thickness (m)	87.5		25–150
		V_S (m/s)	1975		1750–2200
	7	Thickness (m)	500		250–750
		V_S (m/s)	2325		2200–2450
	8	Thickness (m)	1000		500–1500
		V_S (m/s)	2675		2450–2900
	9	Thickness (m)	1500		500–2500
		V_S (m/s)	3050		2900–3200
	10	Thickness (m)	3500		2500–4500
		V_S (m/s)	3250		3200–3300
	SB	V_S (m/s)	3400		3400–3500
IBRH11	1	Thickness (m)	NA[a]	NA[a]	1–3
		V_S (m/s)			100–150
	2	Thickness (m)	10	Fixed	5–10
		V_S (m/s)	170	Initial ± 100%	130–200
	3	Thickness (m)	10	Initial ± 100%	1–15
		V_S (m/s)	240		200–350
	4	Thickness (m)	10		1–25
		V_S (m/s)	450		400–500
	5	Thickness (m)	111		50–250
		V_S (m/s)	2100		1800–2200
	6	Thickness (m)	1914		1–100
		V_S (m/s)	3200		2200–2900
	7	Thickness (m)	5000		500–1500
		V_S (m/s)	3300		2900–3200
	SB	V_S (m/s)	3400		3400

[a] *NA* not-applied, 6 layers over SB were used

Table 4 The correlations used by each code for V_P, density, and damping ratio

Station	Parameter	HHS[a]	TEA[b]
KRD, SLS, SPZ	V_P (m/s)	$\begin{cases} (1.9V_S + 371.57)(1.81 - 6.48 \times 10^{-4}V_S) & depth \leq 25m \\ (1.42V_S + 1162.9)(1.26 - 7.10 \times 10^{-5}V_S) & depth > 25m \end{cases}$	$\begin{cases} (1.06V_S + 436.7) & V_S \leq 400m/s \\ (1.39V_S + 1189.4) & V_S > 400m/s \end{cases}$
	Density (kg/m³)	$1000\left(1.4 + 0.67\sqrt{\frac{V_S}{1000}}\right)$	$\begin{cases} 1000 + \dfrac{1530(V_S/1000)^{0.85}}{(0.35+1.889(V_S/1000)^{1.70})} & V_S \leq 300m/s \\ (1740v_P^{0.25}) & V_S > 300m/s \end{cases}$ $v_P = 0.9409 + 2.0947(V_S/1000) - 0.8206(V_S/1000)^2 + 0.2683(V_S/1000)^3 - 0.0251(V_S/1000)^4$
	Damping ratio (D)	$\frac{5}{V_S \times f}$ *where f is frequency in Hz*	$\frac{5}{V_S \times f}$ *where f is frequency in Hz*
IBRH11	V_P (m/s)	$\begin{cases} (1.9V_S + 371.57)(1.81 - 6.48 \times 10^{-4}V_S) & depth \leq 10m \\ (1.42V_S + 1162.9)(1.26 - 7.10 \times 10^{-5}V_S) & depth > 10m \end{cases}$	$\begin{cases} (1.9V_S + 371.57) & V_S \leq 200m/s \\ (1.42V_S + 1162.9) & V_S > 200m/s \end{cases}$
	Density (kg/m³)	$1000\left(1.4 + 0.67\sqrt{\frac{V_S}{1000}}\right)$	$\begin{cases} 1000 + \dfrac{1530(V_S/1000)^{0.85}}{(0.35+1.889(V_S/1000)^{1.70})} & V_S \leq 200m/s \\ (1740v_P^{0.25}) & V_S > 200m/s \end{cases}$ $v_P = 0.9409 + 2.0947(V_S/1000) - 0.8206(V_S/1000)^2 + 0.2683(V_S/1000)^3 - 0.0251(V_S/1000)^4$
	Damping ratio (D)	$\frac{5}{V_S}$	$\frac{5}{V_S}$

[a] Nagashima and Kawase (2021)

[b] Ashayeri et al. (2023)

tends to yield closer matching with the target eHVSR, while wider deviation from the initial velocity profile in IBRH11. Analogously, TEA tends to remain closer to the initial information from the deep earth structure in cases of the ISMN stations. This means that it is probably rather a matter of choice, not an inherent difference of the two methods.

Soil nonlinearity observed by eHVSR of mainshock

The eHVSR curve of earthquake records with PGA less than 50 cm/s^2 is related to S-wave and P-wave transfer functions of the linear ground response as shown in Eq. 2. It is expected that the strong motions with high PGA values in horizontal components, to generate larger shear strain in soil layers and cause the shear modulus degradation. Hence, recalculation of eHVSR for the earthquake

records of high PGA values can help to show the nonlinear ground response. This was demonstrated from the observations of KiK-net and K-NET stations (Noguchi and Sasatani (2011), Regnier et al. (2013), Ren et al. (2017), and Wang et al. (2021)).

In this section, the eHVSR curves of the mainshock of the earthquake Mw 7.3 on November 12, 2017, at about 36 km from SPZ and 70 km from KRD are reported. The mainshock eHVSR curves for KRD and SPZ are presented in Fig. 4a–b, respectively. It is assumed that DFC is applicable for the mainshock of a single earthquake record, because the high-frequency (larger than 1 Hz) motions are coming from different directions by the scattering inside the seismogenic zone and therefore are forming a quasi-diffuse wave-field. We considered that because of the duration of 20.48 or 40.96 s used for eHVSR analysis, 1 Hz and higher components would have 20–40 times or more pulse summations, which may be sufficient to get
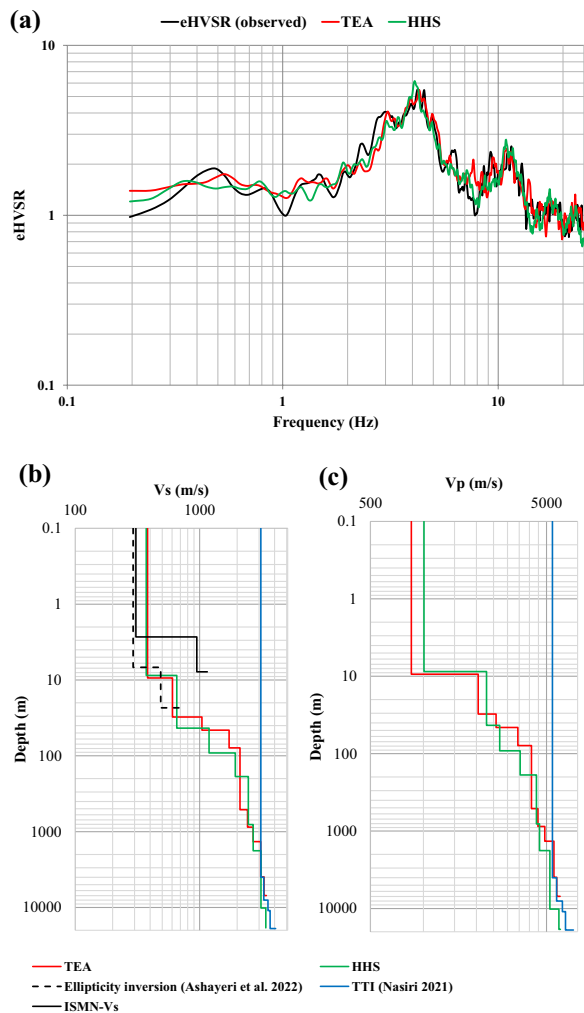

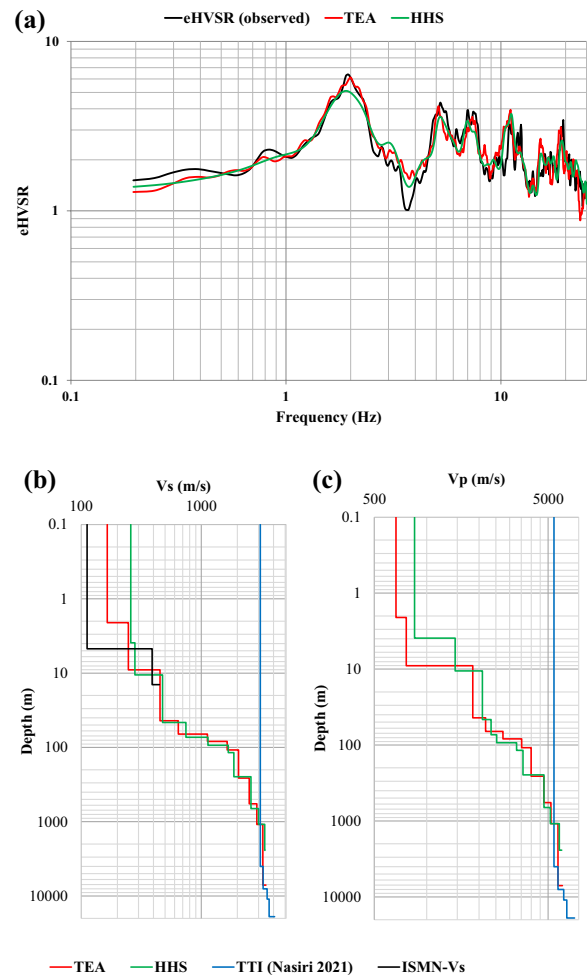**Fig. 6** The least misfit eHVSR curves for KRD (**a**); the corresponding velocity structure by HHS and TEA (**b**, **c**)

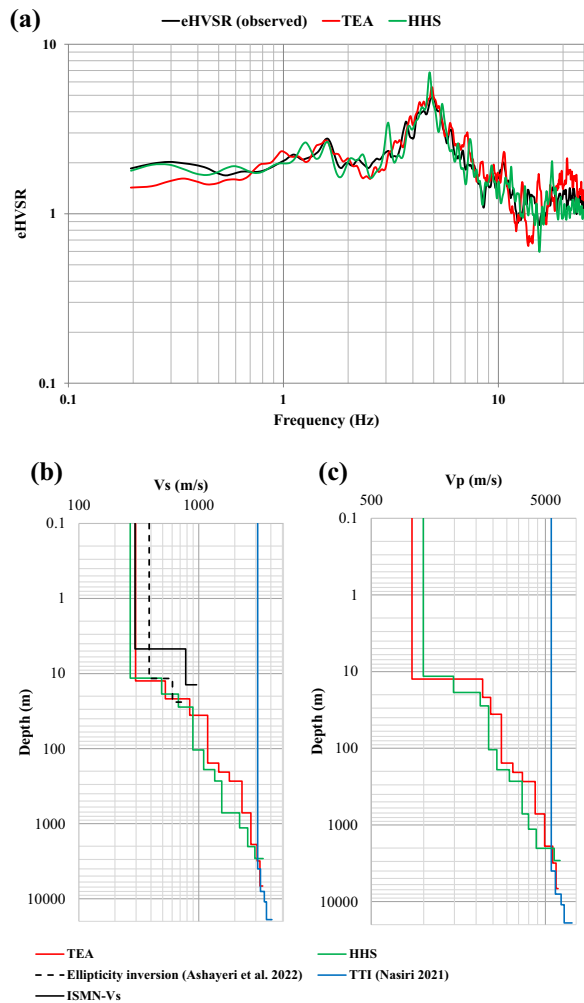**Fig. 7** The least misfit eHVSR curves for SLS (**a**); the corresponding velocity structure by HHS and TEA (**b**, **c**)

Ashayeri *et al. Earth, Planets and Space*   (2023) 75:94

Page 13 of 17

Fig. 8 The least misfit eHVSR curves for SPZ (**a**); the corresponding velocity structure by HHS and TEA (**b**, **c**)

Fig. 9 The least misfit eHVSR curves for IBRH11 (**a**); the corresponding velocity structure by HHS and TEA (**b**, **c**)

a quasi-diffusive status. The mainshock eHVSR curve at each station along with the ground structure of the linear response (from the previous section), is used to search for the V_S reduction in soil layers. For these analyses, we assumed that the V_P structure remains intact, and just the V_S structure of the upper layers exhibit the soil nonlinearity with respect to shear strain. The layers that are contributing to the nonlinearity were determined by a few trials that are limited to the layers with V_S less than 1800 m/s. The trials were set such that the V_S of the layer can take values less than the specified values from the linear eHVSR inversion, and V_S of 1800 m/s well represents a rock layer where the shear strain is adequately low. Please note that probably any layers with V_S higher than 1000 m/s would not become nonlinear, however, we included those stiff layers to confirm that we can obtain similar Vs values for such layers in the inversion for the mainshock eHVSR. Figures 10a and 11a present the least misfit eHVSR curves
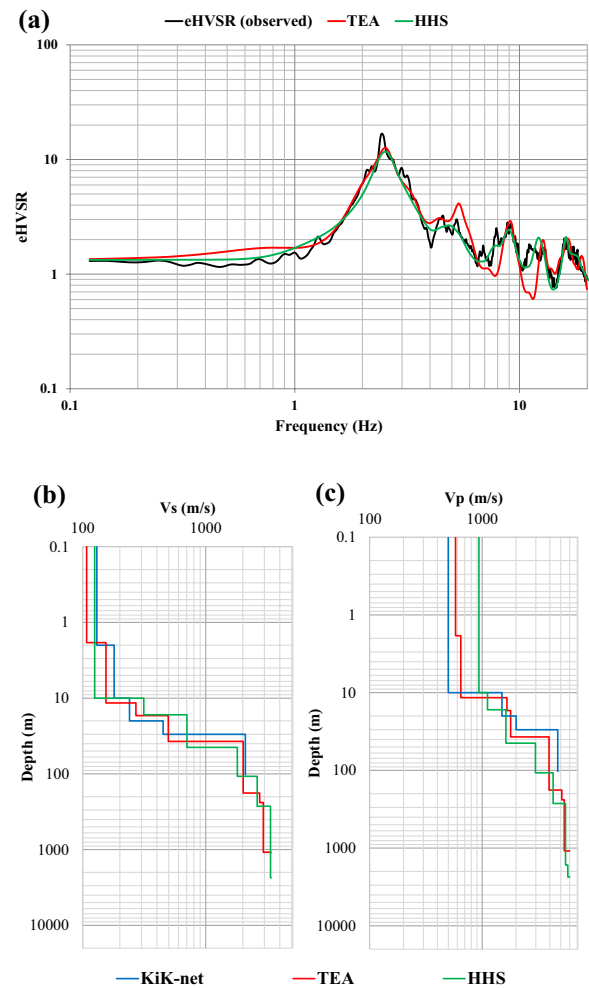
for the mainshock, and Figs. 10b and 11b present the V_S structures of KRD and SPZ during the mainshock compared with those of linear response, respectively. It is observed that V_S is reduced in some layers considerably, to represent the peak frequency shift to lower values, and eHVSR amplitudes that are amplified or de-amplified. The frequency shift as well as amplification and de-amplification along the frequency range is better demonstrated in Figs. 10c and 11c, in which the spectral ratio of the mainshock eHVSR and linear eHVSR is calculated. This spectral ratio is related to the nonlinear site amplification function (NSAF), as it is embedded in Eqs. 3 as an alternative representation of Eq. 2 discussed by Kawase et al. (2018b):

$$eHVSR = \frac{HSAF}{VSAF^*} = \frac{HSAF}{VSAF \cdot \sqrt{\frac{\beta_{SB}}{\alpha_{SB}}}}, \tag{3a}$$

$$NSAF = \frac{eHVSR_{main-shock}}{eHVSR_{linear}} = \frac{HSAF_{nonlinear}}{HSAF_{linear}}, \quad (3b)$$

where HSAF is the horizontal site amplification factor and VSAF is the vertical site amplification factor. VSAF* is a factor that is defined as the amplification of the vertical motion at the surface with respect to the horizontal motion at seismic bedrock (SB). The VSAF* is theoretically equal to VSAF multiplied by the square root of the ratio of S-wave and P-wave velocities at seismic bedrock due to energy partitioning in a Poisson's solid half-space.

It is worth noting that the prominent peak of mainshock eHVSR in SPZ in Fig. 11a at about 0.8 Hz would be related to the source characteristics and the forward directivity effect due to the close distance between SPZ and the epicenter. The epicenter of the mainshock of M_W 7.3 is shown in Fig. 1 along with the location of SPZ on the fault-line, and just 36 km south of the epicenter.

Conclusions

The application of DFC for the earthquakes was well investigated for the strong motions of Japan and their tectonic and geological setting. It is very important to examine DFC for the earthquakes at other tectonic and geological setting. This study presents the first application of DFC on the earthquakes of Iran. The seismic activity of Kermanshah region in the west of Iran, is mostly due to the collision of Arabian plate and Eurasian plate that generated faulting zones along the borders between Turkey and Iran as well as Iraq and Iran. In this study, we investigated three ISMN's stations (i.e., KRD, SLS, SPZ) that are close to the epicenter of a recent November 12, 2017 Mw 7.3 in Iran. A KiK-net
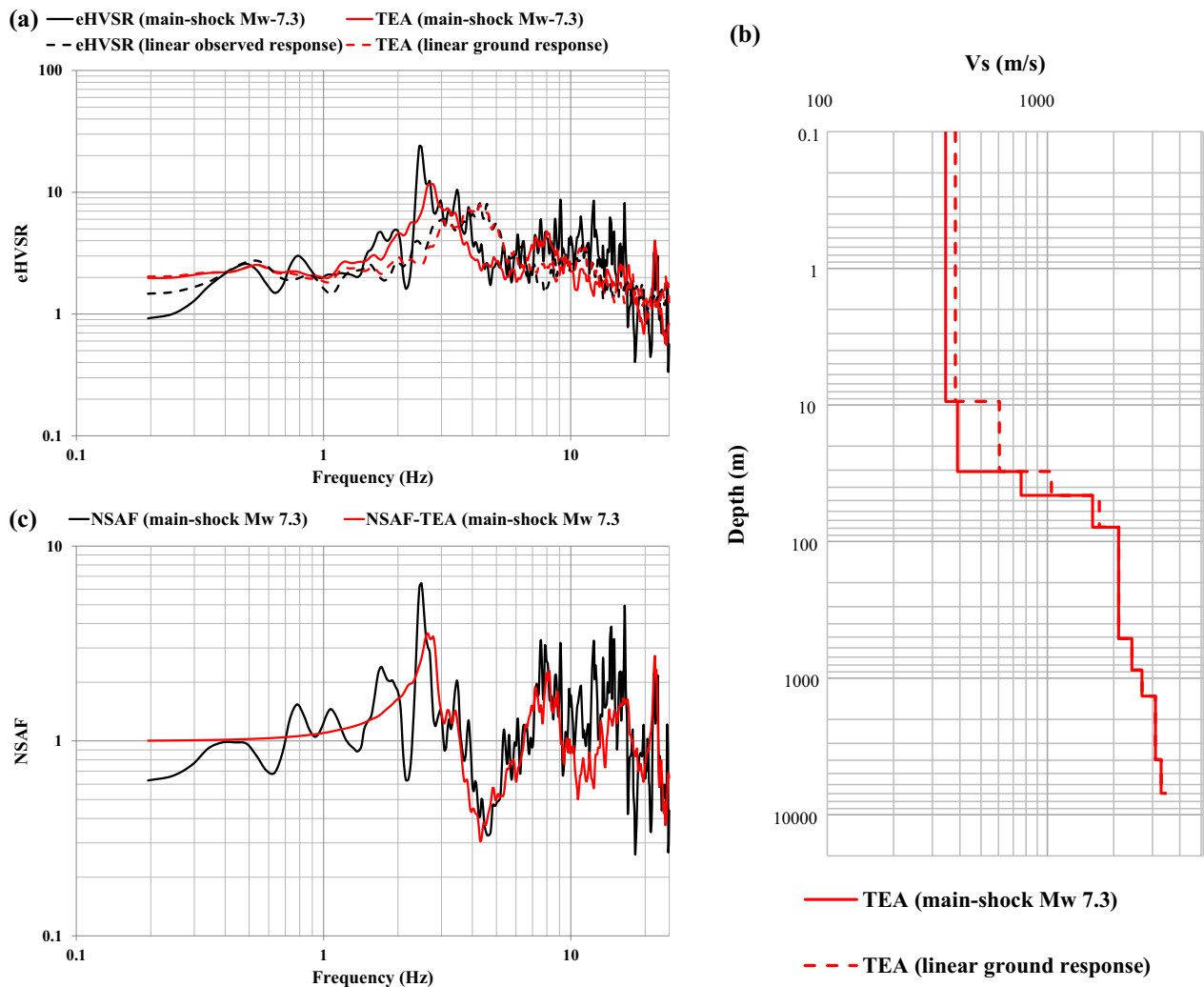

Fig. 10 Nonlinear ground response for KRD, **a** mainshock eHVSR curves (**b**) modified V_S structure and the versus the linear V_S structure, **c** the nonlinear site amplification function
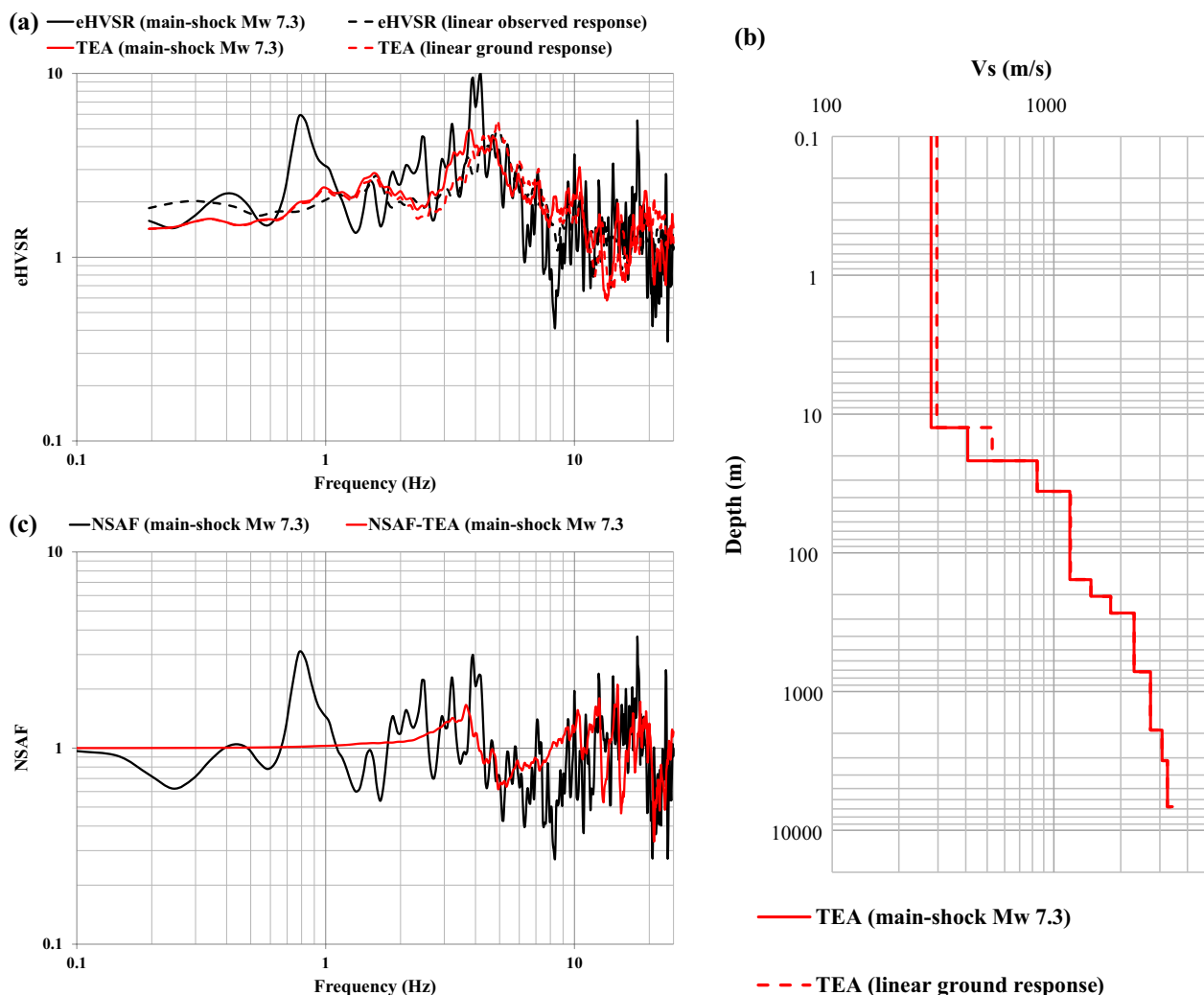
Ashayeri *et al. Earth, Planets and Space*   (2023) 75:94

Page 15 of 17

Fig. 11 Nonlinear ground response for SPZ, **a** mainshock eHVSR curves (**b**) modified V_S structure and the versus the linear V_S structure, **c** the nonlinear site amplification function

station (IBRH11) was studied as a benchmark, too. We performed comparisons of the only two existing velocity structure inversion computer codes based on DFC for earthquakes, i.e., Nagashima et al. (2014) and Ashayeri et al. (2023). The benchmark of IBRH11 showed that the codes are identical in their theoretical eHVSR calculation. This study revealed that the differences between the codes are acceptable for ISMN stations as well as IBRH11, and are caused by differences in search space parameterization and error minimization. The results of this study are very important for ISMN stations, where they are also compared with the shallow velocity structure by Ashayeri et al. (2022) based on the inversion of the ellipticity curve of Rayleigh wave, and the deep velocity structure by Nasiri (2021) based

on the travel time inversion of mainshocks and aftershocks in the region. The results provide reliable velocity structures for the ISMN stations of this study from the ground level to the seismological bedrock that were not available previously. The codes of Nagashima et al. (2014) and Ashayeri et al. (2023) could provide physically meaningful and consistent velocity structures for the ISMN stations. Furthermore, this study provided the V_S structures corresponding to the nonlinear response of KRD and SPZ from the mainshock eHVSR, which represented a frequency shift to lower values and amplification or de-amplification by the soil nonlinearity. This was also important because it showed the successful application of DFC to a single earthquake in the tectonic region of Kermanshah and the calculation of

Ashayeri *et al. Earth, Planets and Space*   (2023) 75:94

Page 16 of 17

the empirical nonlinear site amplification function at these sites.

Abbreviations

DFC	Diffuse field concept
eHVSR	Earthquake horizontal-to-vertical spectral ratio
HHS	Hybrid heuristic search
HSAF	Horizontal site amplification function
ISMN	Iranian Strong Motion Network
NIED	National Research Institute for Earth Science and Disaster Prevention
NSAF	Nonlinear site amplification function
TEA	Telescopic evolutionary algorithm
TTI	Travel time inversion
VSAF	Vertical site amplification function
VSAF[*]	Amplification function of vertical motion at surface of a site with respect to the horizontal motion at seismic bedrock

Availability of data and materials
Earthquake records at KRD, SLS, and SPZ stations were provided by the ISMN (https://ismn.bhrc.ac.ir) freely, as well as IBRH11 by NIED (https://www.kyoshin.bosai.go.jp/kyoshin/db/index_en.html?all). All the other data generated during this study can be disclosed upon request.

Declarations

Ethics approval and consent to participate
Not applicable.

Consent for publication
Not applicable.

Competing interests
The authors declare that they have no competing interests.

Author details
[1]Civil Engineering Department, Razi University, Kermanshah, Iran. [2]Disaster Prevention Research Institute, Kyoto University, Gokasho, Uji, Japan.

References
Aoi S, Asano Y, Kunugi T, Kimura T, Uehira K, Takahashi N, Ueda H, Shiomi K, Matsumoto T, Fujiwara H (2020) MOWLAS: NIED observation network for earthquake, tsunami and volcano. Earth Planets Space. https://doi.org/10.1186/s40623-020-01250-x

Arai H, Tokimatsu K (2004) S-wave velocity profiling by inversion of microtremor H/V spectrum. B Seismol Soc Am 94:53–63. https://doi.org/10.1785/0120030028

Ashayeri I, Sadr A, Biglari M, Haghshenas E (2020) Comprehensive ambient noise analyses for seismic microzonation of sarpol-e-zahab after the Mw 7.3 2017 Iran earthquake. Eng Geol. https://doi.org/10.1016/j.enggeo.2020.105636

Ashayeri I, Memari MA, Haghshenas E (2021) Seismic microzonation of sarpol-e-zahab after Mw 7.3 2017 Iran earthquake: 1D-equivalent linear approach. B Earthq Eng 19:605–622. https://doi.org/10.1007/s10518-020-00999-6

Ashayeri I, Shahvar MP, Moghofeie A (2022) Seismic characterization of Iranian strong motion stations in Kermanshah province (Iran) using single-station Rayleigh wave ellipticity inversion of ambient noise measurements. B Earthq Eng 20:3739–3773. https://doi.org/10.1007/s10518-022-01370-7

Ashayeri I, Nagashima F, Kawase H, Dashti MT (2023) Application of a telescopic evolutionary algorithm with the diffuse-field concept for velocity inversion from strong motion data at K-NET and KiK-net stations in the presence of borehole and geological data. Soil Dyn Earthq Eng. https://doi.org/10.1016/j.soildyn.2022.107528

Biglari M, Formisano A (2020) Damage probability matrices and empirical fragility curves from damage data on masonry buildings after sarpol-e-zahab and bam earthquakes of Iran. Front Built Environ. https://doi.org/10.3389/fbuil.2020.00002

Biglari M, Formisano A, Hashemi BH (2021) Empirical fragility curves of engineered steel and RC residential buildings after Mw 7.3 2017 sarpol-e-zahab earthquake. B Earthq Eng 19:2671–2689. https://doi.org/10.1007/s10518-021-01090-4

Egle DM (1981) Diffuse wave fields in solid media. J Acoust Soc Am 70:476–480

Fäh D, Wathelet M, Kristekova M, Havenith H, Endrun B, Stamm G, Poggi V, Burjanek J, Cornou C. (2009) Using ellipticity information for site characterization. NERIES deliverable JRA4-D4.

García-Jerez A, Luzón F, Sánchez-Sesma FJ, Lunedei E, Albarello D, Santoyo MA, Almendros J (2013) Diffuse elastic wavefield within a simple crustal model. Some consequences for low and high frequencies. J Geophys Res-Sol Ea 118:5577–5595. https://doi.org/10.1002/2013JB010107

García-Jerez A, Piña-Flores J, Sánchez-Sesma FJ, Luzón F, Perton M (2016) A computer code for forward calculation and inversion of the H/V spectral ratio under the diffuse field assumption. Comput Geosci 97:67–78

Hobiger M, Bard PY, Cornou C, Le Bihan N (2009) Single station determination of rayleigh wave ellipticity by using the random decrement technique. Geophys Res Lett. https://doi.org/10.1029/2009GL038863

Hobiger M, Cornou C, Wathelet M, Di Giulio G, Knapmeyer-Endrun B, Renalier F, Bard PY, Savvaidis A, Hailemikael S, Le Bihan N, Ohrnberger M, Theodoulidis N (2013) Ground structure imaging by inversions of rayleigh wave ellipticity: sensitivity analysis and application to European strong-motion sites. Geophys J Int 192:207–229. https://doi.org/10.1093/gji/ggs005

Kawase H, Sanchez-Sesma FJ, Matsushima S (2011) The optimal use of horizontal-to-vertical spectral ratios of earthquake motions for velocity inversions based on diffuse-field theory for plane waves. B Seismol Soc Am 101:2001–2014. https://doi.org/10.1785/0120100263

Kawase H, Mori Y, Nagashima F (2018a) Difference of horizontal-to-vertical spectral ratios of observed earthquakes and microtremors and its application to S-wave velocity inversion based on the diffuse field concept. Earth Planets Space. https://doi.org/10.1186/s40623-017-0766-4

Kawase H, Nagashima F, Nakano K, Mori Y (2018b) Direct evaluation of S-wave amplification factors from microtremor H/V ratios: double empirical corrections to "Nakamura" method. Soil Dyn Earthq Eng. https://doi.org/10.1016/j.soildyn.2018.01.049

Konno K, Ohmachi T (1998) Ground-motion characteristics estimated from spectral ratio between horizontal and vertical components of microtremor. B Seismol Soc Am 88:228–241. https://doi.org/10.1785/BSSA0880010228

Matsushima S, Kosaka H, Kawase H (2017) Directionally dependent horizontal-to-vertical spectral ratios of microtremors at Onahama, Fukushima, Japan. Earth Planets Space. https://doi.org/10.1186/s40623-017-0680-9

Ashayeri *et al. Earth, Planets and Space*   (2023) 75:94

Page 17 of 17

Nagashima F, Kawase H (2021) The relationship between Vs, Vp, density and depth based on PS-logging data at K-NET and KiK-net sites. Geophys J Int 225:1467–1491. https://doi.org/10.1093/gji/ggab037

Nagashima F, Matsushima S, Kawase H, Sánchez-Sesma FJ, Hayakawa T, Satoh T, Oshima M (2014) Application of horizontal-to-vertical (H/V) spectral ratios of earthquake ground motions to identify subsurface structures at and around the K-NET site in Tohoku, Japan. B Seismol Soc Am 104:2288–2302

Nagashima F, Kawase H (2019) Subsurface structure identification based on H/V ratio and surface to borehole ratio. In: Silvestri F, Moraci N (eds). Proceedings of 7th International Conference on Earthquake Geotechnical Engineering. Rome

Nasiri F. (2021). Seismicity of the Western Zagros based on aftershocks analysis of the November 2017 Sarpol-e Zahab earthquake (Mw=7.3). Dissertation, International Institute of Earthquake Engineering and Seismology.

National Research Institute for Earth Science and Disaster Resilience (2019), NIED K-NET, KiK-net, National Research Institute for Earth Science and Disaster Resilience. https://doi.org/10.1759/NIED.0004

Iranian Strong Motion Network, ISMN, https://smd.bhrc.ac.ir/Portal/en. Accessed 20 August 2022.

Nissen E, Ghods A, Karasözen A, Elliott JR, Barnhart WD, Bergman EA, Gavin PH, Jamal-Reyhani M, Nemati M, Tan F, Abdulnaby W, Benz HM, Shahvar MP, Talebian M, Chen L (2019) The 12 November 2017 Mw 7.3 Ezgeleh-Sarpolzahab (Iran) earthquake and active tectonics of the Lurestan arc. J Geophys Res-Sol Ea 124:2124–2152. https://doi.org/10.1029/2018JB016221

Noguchi S, Sasatani T (2011) Nonlinear soil response and its effects on strong ground motions during the 2003 Miyagi-Oki intraslab earthquakes. Zishin 63:165–187

Regnier J, Cadet H, Bonilla LF, Bertrand E, Semblat JF (2013) Assessing nonlinear behavior of soils in seismic site response: statistical analysis on KiK-net strong-motion data. B Seismol Soc Am 103:1750–1770

Ren Y, Wen R, Yao X, Ji K (2017) Five parameters for the evaluation of the soil nonlinearity during the Ms80 wenchuan earthquake using the HVSR method. Earth Planets Space 69:116. https://doi.org/10.1186/s40623-017-0702-7

Sánchez-Sesma FJ, Rodríguez M, Iturrarán-Viveros U, Luzón F, Campillo M, Margerin L, García-Jerez A, Suarez M, Santoyo MA, Rodríguez-Castellanos A (2011a) A theory for microtremor H/V spectral ratio: application for a layered medium. Geophys J Int 186:221–225. https://doi.org/10.1111/j.1365-246X.2011.05064.x

Sánchez-Sesma FJ, Weaver RL, Kawase H, Matsushima S, Luzón F, Campillo M (2011b) Energy partitions among elastic waves for dynamic surface loads in a semi-infinite solid. B Seismol Soc Am 101:1704–1709. https://doi.org/10.1785/0120100196

Satoh T, Kawase H, Iwata T, Higashi S, Sato T, Irikura K, Huang H (2001) S-wave velocity structure of the taichung basin, taiwan, estimated from array and single-station records of microtremors. B Seismol Soc Am 91:1267–1282. https://doi.org/10.1785/0120000706

Satoh T, Hayakawa T, Oshima M, Kawase H, Matsushima S, Nagashima F, Tobita K (2014) Site effects on large ground motions at KiK-net iwase station IBRH11 during the 2011 Tohoku earthquake. B Seismol Soc Am 104:653–668. https://doi.org/10.1785/0120130095

Wang Z, Nagashima F, Kawase H (2021) A new empirical method for obtaining horizontal site amplification factors with soil nonlinearity. Earthq Eng Struct D 50:2774–2794. https://doi.org/10.1002/eqe.3471

Weaver RL (1982) On diffuse waves in solid media. J Acoust Soc Am 71:1608–1609

Weaver RL (1985) Diffuse elastic waves at a free surface. J Acoust Soc Am 78:131–136

Yamanaka H (2007) Inversion of surface-wave phase velocity using hybrid heuristic search method. Butsuri-Tansa 60(3):265–275. https://doi.org/10.3124/segj.60.265

Publisher's Note

Springer Nature remains neutral with regard to jurisdictional claims in published maps and institutional affiliations.